Supplementary Information

Effect of Nanoparticles on the Bulk Shear Viscosity of a Lung Surfactant Fluid

Le-Phuong-Anh Thai, Fanny Mousseau, Evdokia Oikonomou, Milad Radiom and Jean-François Berret*

Outline

Movie#1 – Movie of a 43 µm magnetic wire undergoing a synchronous motion (at the angular frequency of 0.06 rad s^{-1} and under a magnetic field $\mu_0 H$ of 10.3 mT) in a 44 g L^{-1} pulmonary surfactant dispersion loaded with alumina nanoparticles (c_{NP} = 0.004 g L^{-1}). The time evolution of the wire orientation is displayed in Fig. 2b.

Movie#2 – Same as Movie#1 at the angular frequency of 3.0 rad s^{-1}. The time evolution of the wire orientation is displayed in Fig. 2d.

Movie#3 – Movie of a 64 µm magnetic wire undergoing back-and-forth oscillations (at the angular frequency of 0.06 rad s^{-1} and under a magnetic field $\mu_0 H$ of 10.3 mT) in a 44 g L^{-1} pulmonary surfactant dispersion loaded with alumina nanoparticles (c_{NP} = 0.40 g L^{-1}). The time evolution of the wire orientation is displayed in Fig. 4b.

Movie#4 – Same as Movie#3 at the angular frequency of 3.0 rad s^{-1}. The time evolution of the wire orientation is displayed in Fig. 4d.

Movie#5 – Combined movies showing pristine Curosurf® at 44 g L^{-1} (left) and Curosurf® at the same lipid concentration loaded with alumina (center) and silica (right) particles (c_{NP} = 0.50 g L^{-1}). The absence of fluctuations for the sample containing alumina is interpreted as an evidence of an arrested state induced by the particles.

Keywords: Pulmonary (lung) surfactant – Nanoparticles – Biomolecular corona – Magnetic wires – Microrheology
Corresponding authors: jean-francois.berret@univ-paris-diderot.fr

Revised version submitted to ACS Nano
Thursday, December 19, 19

Supplementary Information S1
Curosurf® composition and comparison with the native surfactant

Lipid composition (%, g/g of total lipid)	Native Surfactant	Curosurf
Phosphatidylcholine (PC)	70 - 85	67 - 74
Lysophosphatidyl choline (LPC)	0.5	< 1
Sphingomyelin (SM)	2	8.1
Cholesterol	5	0
Phosphatidylinositol (PI)	4 – 7	3.3
Phosphatidylserine (PS)	5	
Phosphatidylethanolamine (PE)	3	4.5
Phosphatidylglycerol (PG)	7 – 10	1.2
Protein concentration (%, g/g of total lipid)	**Native Surfactant**	**Curosurf**
SP-A	4	0
SP-B	1	0.3
SP-C	1	0.7
SP-D	4	0

Table S1: Lipid and protein compositions of native surfactant obtained by saline bronchoalveolar lavage compared to that of Curosurf®, a pulmonary surfactant substitute indicated for the rescue treatment of Respiratory Distress Syndrome (RDS) in premature infants.[1] The concentrations are given in percentage by weight of the total lipid content.

Supplementary Information S2
Fluid-to-Gel transition from the Curosurf® phospholipid bilayer

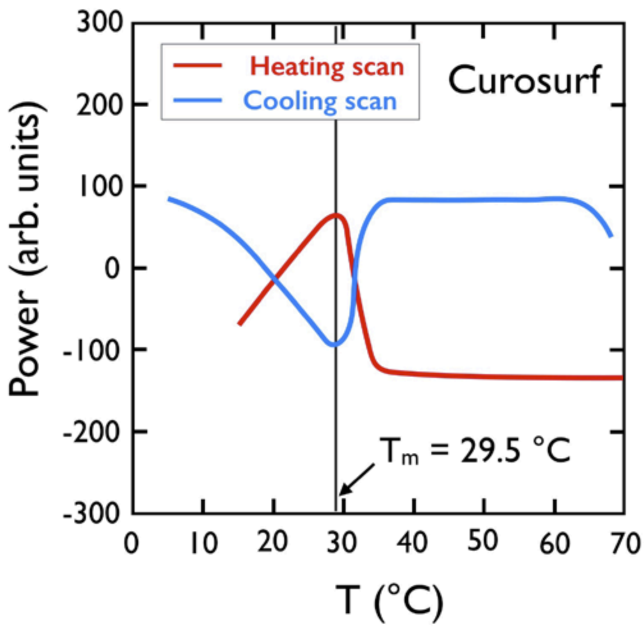

Figure S2: Thermograms of Curosurf® diluted in DI-water at 10 g L^{-1} obtained by differential scanning calorimetry (DSC). The Curosurf® bilayer melting temperature was estimated at T_m = 29.5 °C from heating and cooling cycles.[2] Thermograms were measured using an N-DSCIII instrument from CSC. The reference cell was filled with DI-water and the sample cell (0.3 mL) with Curosurf®. The capillary cells were not capped and a constant pressure of 5×10^5 Pa was applied. The transition temperature was taken at the second, third and fourth heating scans, at a scan rate of 0.5 °C min^{-1} (from 5 to 70 °C). The melting temperature was estimated as the mean of the three temperatures mentioned before, leading to T_m = 29.5 °C.[3] The same procedure was applied with the cooling scans, which were performed in the same conditions.

Supplementary Information S3

Dynamic light scattering on Curosurf®/negative silica nanoparticles

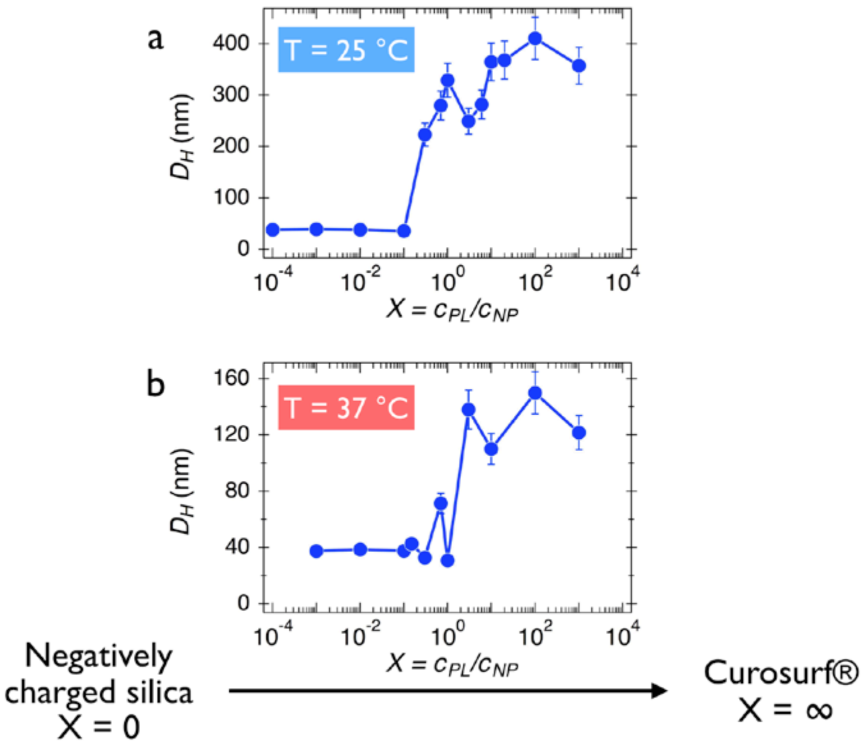

Figure S3: Hydrodynamic diameter of nanoparticle-vesicle dispersions as a function of the concentration ratio $X = c_{PL}/c_{NP}$ obtained from dynamic light scattering at T = 25 °C **(a)** and T = 37 °C **(b)** for 20 nm negatively charged silica. In the figures, X = 0 denotes the nanoparticle dispersion and X = ∞ Curosurf®. The error bars represent the mean of the standard deviations for measurements made in triplicate.

Supplementary Information S4
Additional cryo-TEM images of Curosurf® vesicles

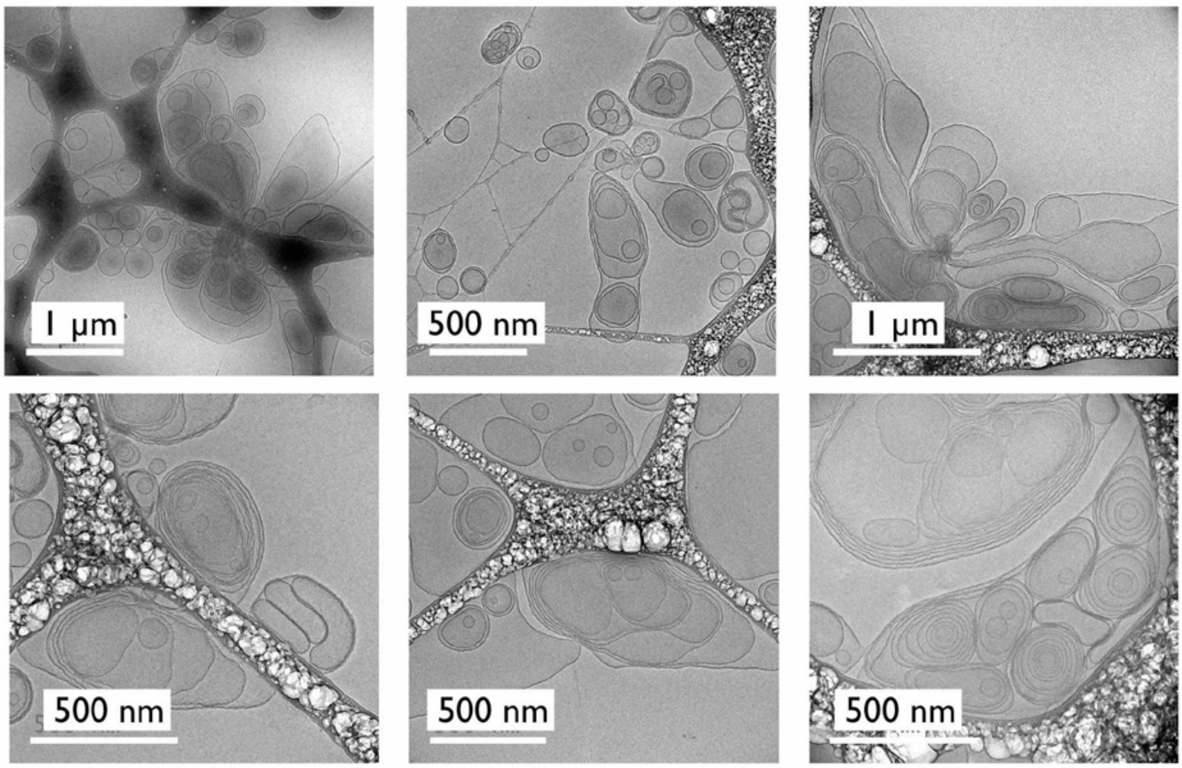

Figure S4: Cryo-TEM images of Curosurf® vesicles at the concentration of 5 g L^{-1}.[2-4]

Supplementary Information S5
Additional oscillation amplitude data for Curosurf® loaded with alumina particles

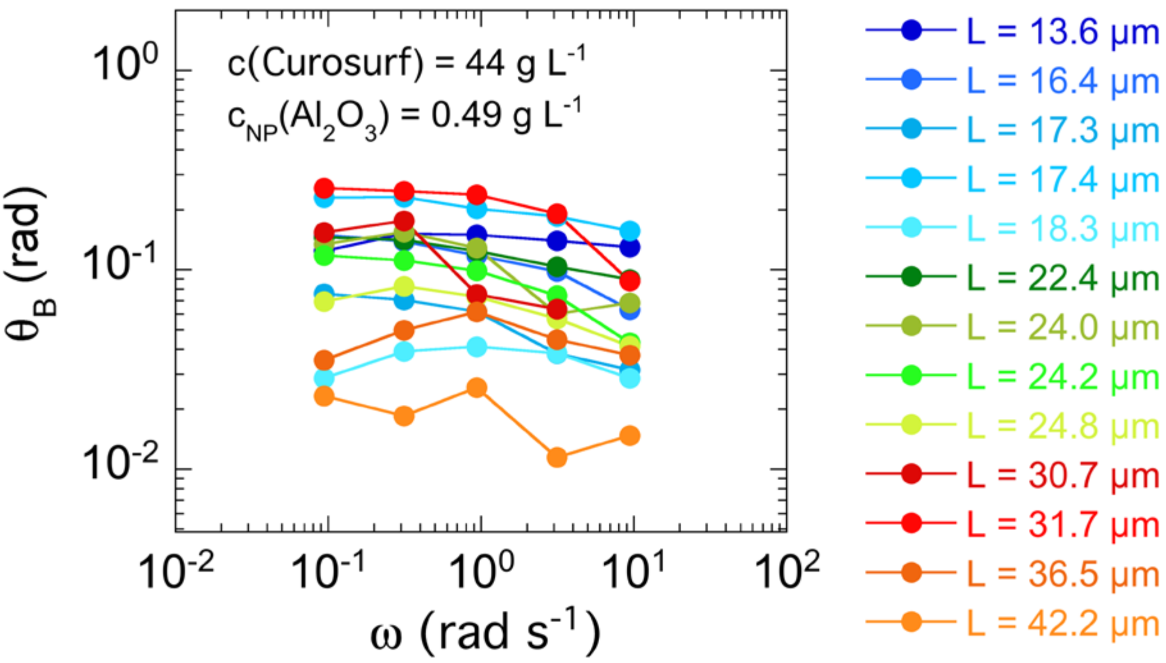

Figure S5: Oscillation amplitude $\theta_B(\omega)$ measured in Curosurf® loaded with alumina particles at c_{NP} = 0.49 g L^{-1} using wires of length between 13 and 42 µm. The $\theta_B(\omega)$-data show an almost flat variation in this frequency range, suggesting a gel-like behavior. For this sample, it is assumed that the alumina particles added to the dispersion stick to the lipid membrane and participate to the formation of the crosslinked vesicular network.

Supplementary Information S6

Transmitted light intensity for Curosurf® without and with nanoparticles

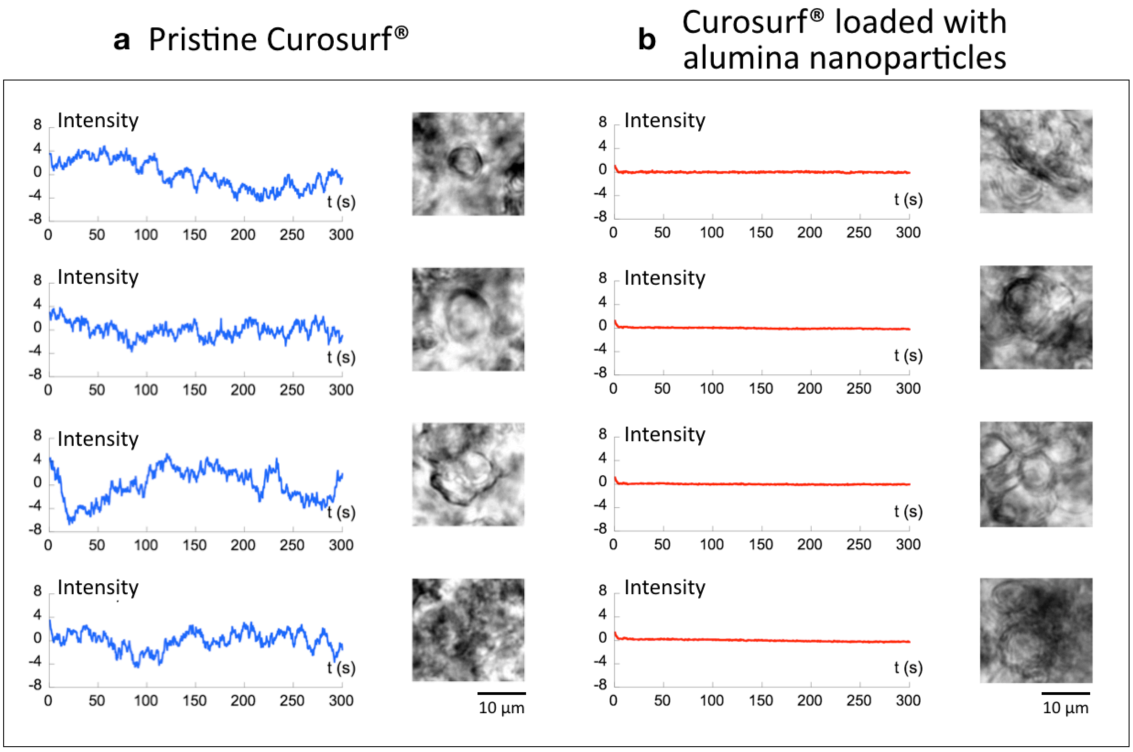

Figure S6: a) Left-hand panels: variations of the transmitted light intensity measured from phase-contrast X40 optical microscopy on a pristine Curosurf® sample. The intensity is determined at different locations in the sample, as shown by the four intensity plots. Right-hand panels: investigated fields of view. **b)** Same as in Fig. S6a for a Curosurf® dispersion loaded with alumina particles at c_{NP} = 0.49 g L^{-1}.

Supplementary Information S7
Mircrorheology data for Curosurf® treated with negatively charged silica

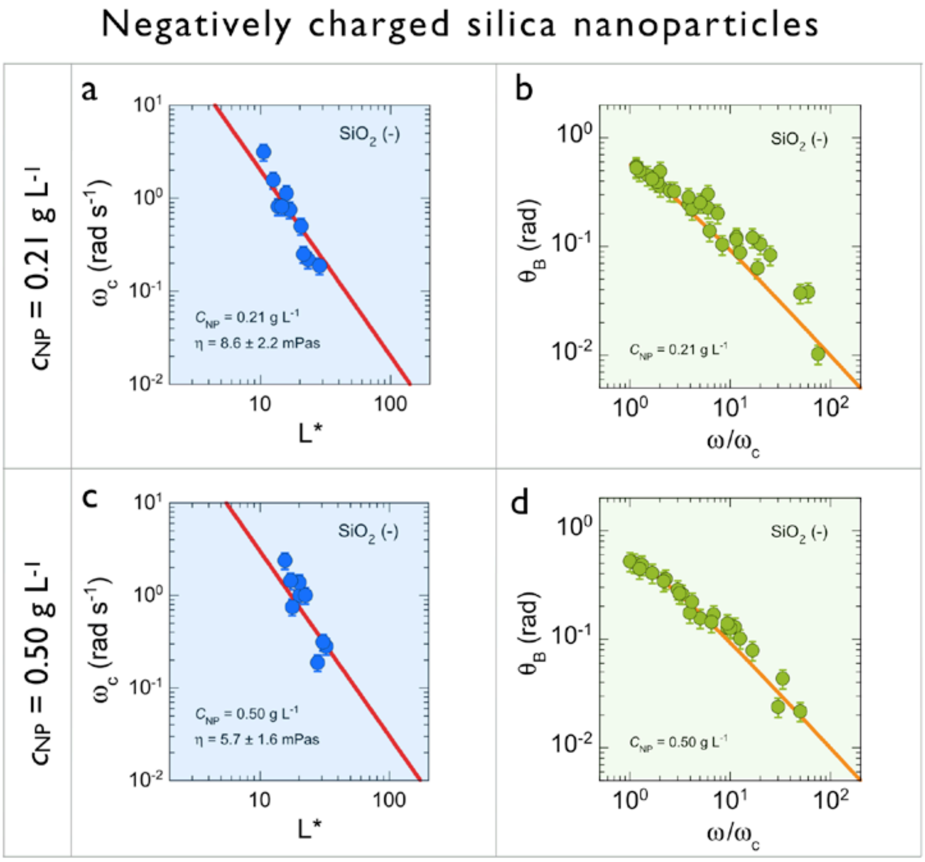

Figure S7: a) and **c)** Critical frequency ω_C as a function of the reduced wire length L^* obtained for Curosurf® dispersions loaded with negative silica particles at concentrations c_{NP} = 0.21 g L^{-1} and c_{NP} = 0.50 g L^{-1}. The Curosurf® concentration is set at the physiological value, 44 g L^{-1}. The straight line displays the $1/L^{*2}$-dependence predicted from the viscous fluid constitutive equation. **b)** and **d)** Oscillation amplitude $\theta_B(\omega/\omega_C)$ observed in the asynchronous regime for the same samples as in **a)** and **c).** The straight line is for Newtonian fluids.

Supplementary Information S8
List of production volumes and industrial applications for silica and alumina nanoparticles for 2012

Silica nanoparticles Production volumes for nanomaterials (2012): 500 000 tons*	**Alumina nanoparticles** Production volumes for nanomaterials (2012): 30 000 tons*
Aerogels as light-weight materials and thermal insulators.	Coatings and paint
Filler in rubber and polymer compound materials	Polishing slurries
Nanoelectronics fabrication as mask substrate	Airbag propellants and energetic materials
Bioceramics (as coatings for implants)	Air purification
Anti-corrosion and wear resistant coatings	Composite reinforcement
Insulators with high dielectric properties	Fuel cells
	Supercapacitor
	Transparent ceramics
	Optoelectronics and military and defense applications
	Polymer composites as solid lubricants
	Pipe material in gas discharge lamps.
	Fuels for space and naval vehicles and propellants for the military
	Cosmetic filler

Table S8: List of silica and alumina nanoparticle applications.[5] (*)The production volumes for nanomaterials for 2012 are averaged between upper and lower estimates. http://www.nanotechmag.com/wp-content/uploads/2014/09/ALUMINIUM-OXIDE-NANOPARTICLES-2013-.pdf

Supplementary Information S9

Curosurf® viscosity as a function of the vesicle volume fraction

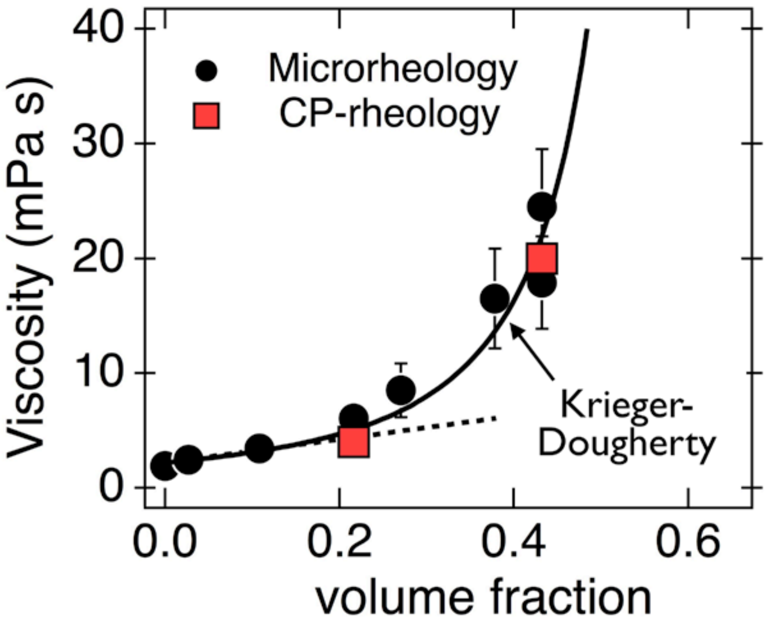

Figure S9: Volume fraction dependence of the Curosurf® static viscosity $\eta(\phi)$. The dashed line is obtained from the Einstein model while the continuous line is derived from the Krieger-Dougherty equation.[6,7] The Krieger-Dougherty displays a viscosity divergence at ϕ = 0.65, corresponding to lipid concentration of 117 g L^{-1}. Note that the data from microrheology and from classical rheometry using a Cone-and-Plate (CP) device are in good agreement.[8]

Supplementary Information S10
Correspondence between the NP concentration in Curosurf® and the amount of nano-particles in the alveolar region

In this section, we provide detailed calculations of the total amount of silica and alumina nano-particles that would be present in the alveolar region of human lungs, assuming NP concentrations in the range 10^{-3} g L^{-1} - 0.5 g L^{-1}. We recall that the first effect on the viscosity occurs at 10^{-2} g L^{-1} for positive silica and alumina, and at 10^{-1} g L^{-1} for the liquid-to-soft solid transition for alumina.

In the following, we base our calculations on human lung figures which are widely accepted by the community (Table S10-1).[9]

Available surface in the alveolar region	S_{AR}	70 m^2
Alveolus diameter	D_{Alv}	200 µm
Thickness of pulmonary surfactant	δ_{PS}	0.2 – 0.5 µm
Total volume of pulmonary surfactant in the lungs	V_{PS}	25 mL
Volume of pulmonary surfactant in an alveolus	v_{PS}	80 pL
Number of alveoli in the lungs	N_{Alv}	300 million

Table S10-1: Size, surface and volume characterizing the alveolar region of the lungs.[9]

The particles are described by their median geometric diameter D_0, the dispersity of the size distribution s and by their mass density ρ. Their number-average molecular weight M_n^{NP} reads:

$$M_n^{NP} = \frac{\pi}{6}\rho D_0^3 exp(4.5s^2)\mathcal{N}_A \qquad (S10-1)$$

where $\mathcal{N}_A$ the Avogadro number. For log-normal distribution of median diameter D_0 and dispersity s, the nth-moment is given by the expression $< D_0^n > = (D_0)^n \exp(n^2s^2/2)$.

In this work, the nanoparticle concentration c_{NP} in the surfactant dispersion is varied from 0.001 g L^{-1} to 0.5 g L^{-1}. Assuming a volume of surfactant per alveolus of v_{PS} = 80 pL (Table S10-1), the mass of particles in a single alveolus and in the alveolar region are respectively:

$$m_{Alv}^{NP} = v_{PS}c_{NP} \qquad (S10-2)$$

$$m_{AR}^{NP} = V_{PS}c_{NP} \qquad (S10-3)$$

The mass m_{Alv}^{NP} can be transformed into a number of particles per alveolus using:

$$N_{Alv}^{NP} = \frac{m_{Alv}^{NP}}{M_n^{NP}} \mathcal{N}_A \qquad (S10-4)$$

Table S10-2 provides the correspondence between the nanoparticle concentrations used in this work and the mass m_{Alv}^{NP} and number N_{Alv}^{NP} of NPs in a single alveolus (Eqs. S10-2&3). In the last column, the total mass of particles in the alveolar region m_{AR}^{NP} is provided (Eqs. S10-3). This later quantity may be of interest for the comparison with actual exposure data.

c_{NP} (g L^{-1})	c_{NP} (µg mL^{-1})	m_{Alv}^{NP} (g)	N_{Alv}^{NP} Silica(+)	N_{Alv}^{NP} Alumina(+)	N_{Alv}^{NP} Silica(-)	m_{AR}^{NP} (µg)
0.001	1	8×10^{-14}	1.1×10^{3}	7.9×10^{2}	8.4×10^{3}	24
0.01	10	8×10^{-13}	1.1×10^{4}	7.9×10^{3}	8.4×10^{4}	240
0.1	100	8×10^{-12}	1.1×10^{5}	7.9×10^{4}	8.4×10^{5}	2400
0.5	500	4×10^{-11}	5.4×10^{5}	3.9×10^{5}	4.2×10^{6}	12000

Table S10-2: Correspondence between the NP concentrations used in this work and the mass of NPs in the alveolar region using the data from Table S10-1 and Eqs. S10-1-4. The calculations are made using ρ = 1900 kg m^{-3} for silica and ρ = 3950 kg m^{-3} for alumina.

Supplementary Information S11
Wire synthesis scheme

Iron oxide nanoparticles (γ-Fe_2O_3) were obtained by co-precipitation of iron(II) and iron(III) salts in aqueous solution according to the Massart synthesis. The particle size (6.8 nm) and dispersity (0.18) were measured by TEM, whereas the maghemite cubic structure was assessed by electron beam diffraction.[10] Light scattering was used to measure the weight-average molecular weight (M_W = 1.3×10^6 g mol^{-1}) and hydrodynamic diameter (D_H = 13 nm) for the bare particles.[10] To be incorporated in larger structures, γ-Fe_2O_3 was coated with poly(acrylic) acid polymers (PAA_{2K}, Aldrich, M_w = 2100 g mol^{-1}) following the precipitation-redispersion method.[11]

The process is based on the dialysis from dispersions containing polymers and particles in an excess of salt (NH_4Cl, Aldrich). For the linear growth of the aggregates, the dialysis bath was placed in a permanent magnetic field of 0.1 Tesla generated by permanent rare-earth neodynium magnets. This method provides large amounts of wires, around 10^{10} per synthesis. Small-angle X-ray scattering has shown that the particles are at close contact, resulting in magnetic volume fractions of about 30%.[11] The wires were also characterized with respect to their mechanical rigidity.[12] It was found that their persistence length was about 1 m and their Young modulus was 3 – 10 MPa, *i.e.* similar to that of elastomers. Under such conditions the wires are rigid and do not exhibit deformation or bending when submitted to steady rotation.

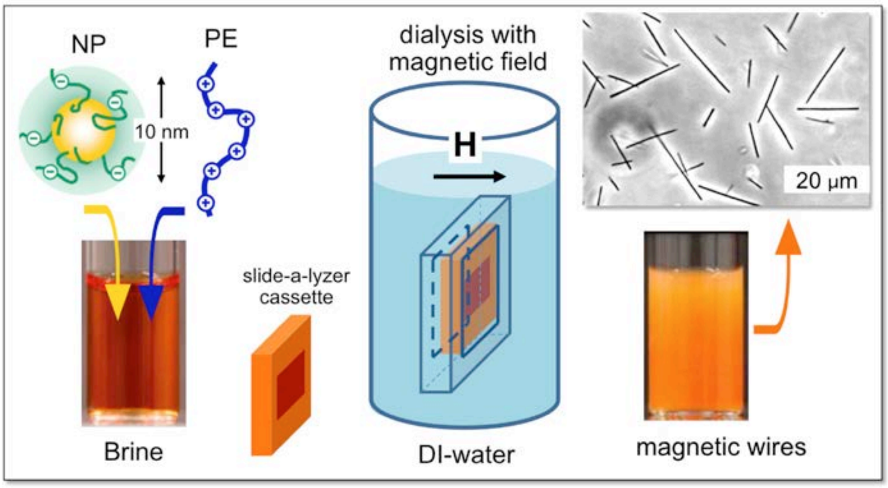

Figure S11: Schematic representation of the protocol that controls the nanoparticle co-assembly and wire formation. The dialysis involves the preparation of separate 1 M NH_4Cl salted solutions of particles and copolymers. The ionic strength is progressively diminished by dialysis with a 10000 g mol^{-1} cut-off Slide-a-Lyzer® cassette.[13]

Supplementary Information S12
Magnetic wire characterization using optical microscopy

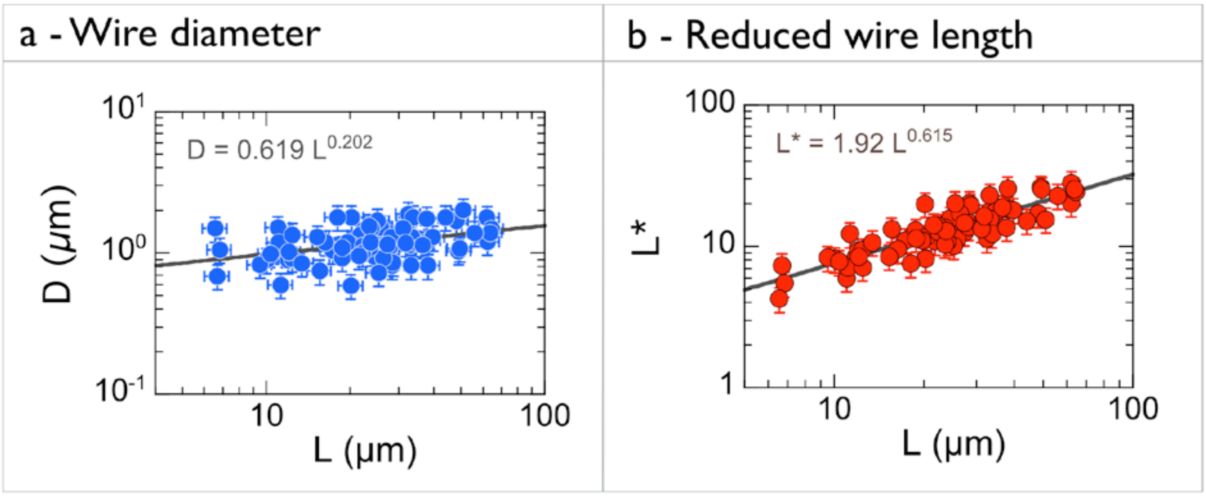

Figure S12: a) Wire diameter measured using optical microscopy (objective X100, numerical aperture 1.3) as a function of the wire length. The observed power law $\mathrm{D} = 0.619\mathrm{L}^{0.202}$ can be understood assuming that wires are actually bundles of thinner rods that stick together during the dialysis process.[8] **b)** Reduced wire length $L^{*}(L,D) = L/D\sqrt{g(L/D)}$ calculated from **a)**. The best fit calculation using a scaling law gives $L^{*}(L) = 1.92L^{0.615}$. This expression is used in Eq. 1 for the water-glycerol solutions and for the Curosurf® suspensions.

Supplementary Information S13
Magnetic field rotating device and spatial distribution of the magnetic field

The magnetic wire microrheology technique has been described in previous accounts.[12,14,15] For reviews on microrheology techniques and data analysis, especially those using anisotropic probes, we refer to Refs[16,17]. We summarize here specific issues related to the sample preparation, measurement protocols and data analysis. Concerning the sample preparation, Curosurf® stock suspensions were used as received and diluted to the desired concentrations of 5, 20, 40, 50, 70 and 80 g L^{-1} using PBS. A total of 10^5 wires (contained in 0.5 µL) was then added to 100 µL of the previous suspensions and gently stirred. Under such conditions the inter-wire distance was larger than their length and the wires did not interact with each other, either magnetically or hydrodynamically. 25 µL of the previous suspension were deposited on a glass plate and sealed into to a Gene Frame® (Abgene/Advanced Biotech, dimensions 10×10×0.25 mm^3). The microrheology protocol is based on the Magnetic Rotational Spectroscopy (MRS) technique. MRS consists in applying a rotating magnetic field to a wire and recording its motion by time-lapse microscopy.[18] The experiment itself used a home-made device operating with two pairs of coils working with a 90°-phase shift, coupled to a frequency generator and an amplifier. Angular frequencies ω from 10^{-3} to 10^2 rad s^{-1} and magnetic fields $\mu_0 H$ from 0 to 20 mTesla were investigated. Stacks of images were acquired from an IX73 Olympus inverted microscope, digitized and treated by the ImageJ software and plugins. In a purely viscous fluid, a wire placed in the MRS configuration experiences a friction torque that tends to slow down its motion. With increasing frequency, the torque increases and above a certain value ω_C, the wire exhibits an asynchronous motion with respect to the field. To improve the experimental accuracy, ω_C is measured from a batch of wires of different lengths and fitted against $L^*(L,D) = L/D\sqrt{g(L/D)}$. The static viscosity is then obtained from the slope of the $\omega_C \sim 1/{L^*}^2$ scaling behavior.

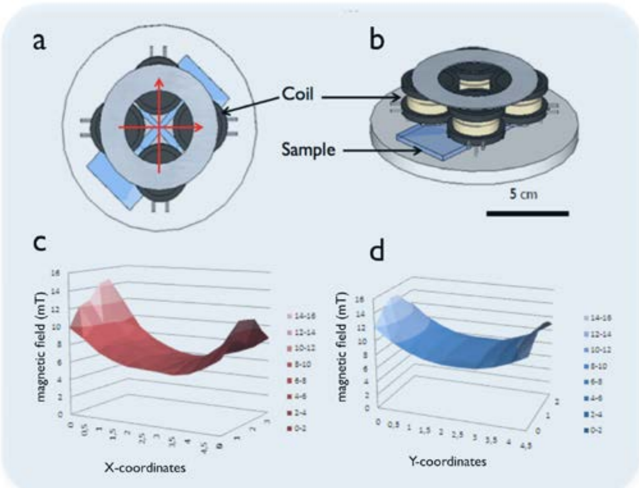

Figure S13: Top (a) and side (b) views of the rotating field device used this work. Magnetic field distributions are shown along the X (c) and Y (d) axis of the four-coil device. In the center, the magnetic field is constant over a 1×1 mm^2 range. With this device, the magnetic field can be varied from 0 to 20 mTesla and the angular frequencies ω from 10^{-3} to 10^2 rad s^{-1}.

Supplementary Information S14

Calibrating the magnetic wires using water-glycerol solutions of different viscosity

To determine the susceptibility parameter $\Delta\chi$ in Eq. 1, MRS was performed on a series of water-glycerol mixtures of increasing viscosities, 4.95, 34.9, 48.9 and 80.0 mPa s, corresponding to glycerol concentrations of 49.8%, 81.0%, 84.5% and 89% (T = 25 °C). The critical frequency was determined experimentally and plotted as a function of L^*, resulting in $\Delta\chi = \chi^2/(2+\chi)$ = 0.056 ± 0.006 and χ = 0.36 ± 0.03.

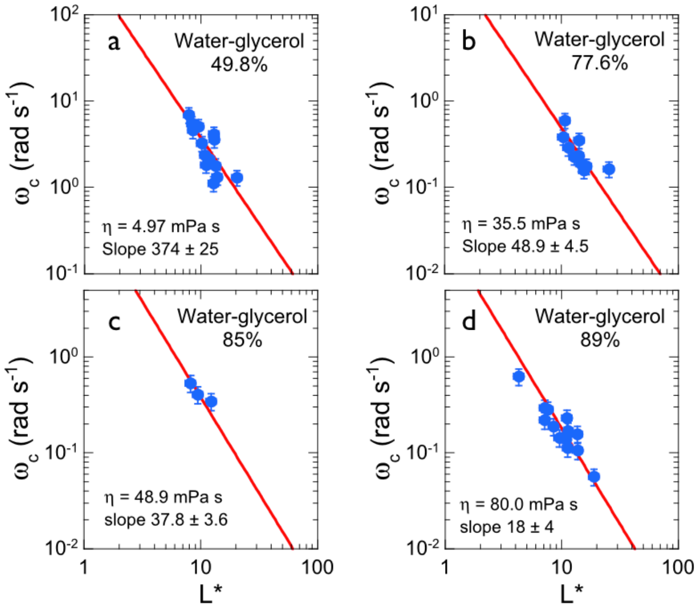

Figure S14: Critical frequency ω_C as a function of the reduced wire length $L^* = L/D\sqrt{g(L/D)}$ obtained for water-glycerol solutions of different concentrations (T = 25 °C).

a) Glycerol concentration 49.8%, viscosity 4.97 mPa s
b) Glycerol concentration 77.6%, viscosity 35.5 mPa s
c) Glycerol concentration 85.0%, viscosity 48.9 mPa s
d) Glycerol concentration 89.0%, viscosity 80.0 mPa s

Straight lines are least-square fits using Eq. 1. The prefactor to the $\omega_C \sim 1/L^{*2}$ scaling is used to calculate the anisotropy of the magnetic susceptibility $\Delta\chi = \chi^2/(2+\chi)$ between parallel and perpendicular directions (with respect to the magnetic field).[12,14] χ is the material magnetic susceptibility.

References

1. Braun, A.; Stenger, P. C.; Warriner, H. E.; Zasadzinski, J. A.; Lu, K. W.; Taeusch, H. W., A Freeze-Fracture Transmission Electron Microscopy and Small Angle X-Ray Diffraction Study of the Effects of Albumin, Serum, and Polymers on Clinical Lung Surfactant Microstructure. *Biophys. J.* **2007,** *93*, 123-139.
2. Mousseau, F.; Le Borgne, R.; Seyrek, E.; Berret, J.-F., Biophysicochemical Interaction of a Clinical Pulmonary Surfactant with Nanoalumina. *Langmuir* **2015,** *31*, 7346-7354.
3. Mousseau, F.; Berret, J. F., The Role of Surface Charge in the Interaction of Nanoparticles with Model Pulmonary Surfactants. *Soft Matter* **2018,** *14*, 5764-5774.
4. Mousseau, F.; Puisney, C.; Mornet, S.; Le Borgne, R.; Vacher, A.; Airiau, M.; Baeza-Squiban, A.; Berret, J. F., Supported Pulmonary Surfactant Bilayers on Silica Nanoparticles: Formulation, Stability and Impact on Lung Epithelial Cells. *Nanoscale* **2017,** *9*, 14967-14978.
5. *The Global Market for Aluminium Oxide Nanoparticles*; Technology report N° 76; Future Markets, Inc.: 2013; http://www.nanotechmag.com/wp-content/uploads/2014/09/ALUMINIUM-OXIDE-NANOPARTICLES-2013-.pdf; Access date: 24 October 2019
6. Krieger, I. M.; Dougherty, T. J., A Mechanism for Non-Newtonian Flow in Suspensions of Rigid Spheres. *Trans. Soc. Rheol.* **1959,** *3*, 137-152.
7. Larson, R. G., *The Structure and Rheology of Complex Fluids*. Oxford University Press: New York, 1998.
8. Thai, L. P. A.; Mousseau, F.; Oikonomou, E. K.; Berret, J. F., On the Rheology of Pulmonary Surfactant: Effects of Concentration and Consequences for the Surfactant Replacement Therapy. *Colloids Surf., B* **2019,** *178*, 337-345.
9. Notter, R. H., *Lung Surfactant: Basic Science and Clinical Applications*. CRC Press: Boca Raton, FL, 2000; Vol. 149.
10. Fresnais, J.; Yan, M.; Courtois, J.; Bostelmann, T.; Bee, A.; Berret, J. F., Poly(Acrylic Acid)-Coated Iron Oxide Nanoparticles: Quantitative Evaluation of the Coating Properties and Applications for the Removal of a Pollutant Dye. *J. Colloid Interface Sci.* **2013,** *395*, 24-30.
11. Berret, J.-F., Controlling Electrostatic Co-Assembly Using Ion-Containing Copolymers: From Surfactants to Nanoparticles. *Adv. Colloids Interface Sci.* **2011,** *167*, 38-48.
12. Chevry, L.; Sampathkumar, N. K.; Cebers, A.; Berret, J. F., Magnetic Wire-Based Sensors for the Microrheology of Complex Fluids. *Phys. Rev. E* **2013,** *88*, 062306.
13. Fresnais, J.; Berret, J.-F.; Frka-Petesic, B.; Sandre, O.; Perzynski, R., Electrostatic Co-Assembly of Iron Oxide Nanoparticles and Polymers: Towards the Generation of Highly Persistent Superparamagnetic Nanorods. *Adv. Mater.* **2008,** *20*, 3877-3881.
14. Berret, J.-F., Local Viscoelasticity of Living Cells Measured by Rotational Magnetic Spectroscopy. *Nat. Commun.* **2016,** *7*, 10134.
15. Loosli, F.; Najm, M.; Chan, R.; Oikonomou, E.; Grados, A.; Receveur, M.; Berret, J.-F., Wire-Active Microrheology to Differentiate Viscoelastic Liquids from Soft Solids. *ChemPhysChem* **2016,** *17*, 4134-4143.
16. Squires, T. M.; Mason, T. G., Fluid Mechanics of Microrheology. *Annu. Rev. Fluid Mech.* **2010,** *42*, 413-438.
17. Tierno, P., Recent Advances in Anisotropic Magnetic Colloids: Realization, Assembly and Applications. *Phys. Chem. Chem. Phys.* **2014,** *16*, 23515-23528.
18. Tokarev, A.; Yatvin, J.; Trotsenko, O.; Locklin, J.; Minko, S., Nanostructured Soft Matter with Magnetic Nanoparticles. *Adv. Funct. Mater.* **2016,** *26*, 3761-3782.